Physics in Medicine & Biology

IPEM Institute of Physics and Engineering in Medicine

PAPER • OPEN ACCESS

Uncertainty analysis in hyperthermia treatment planning for head & neck cancer using polynomial Chaos expansion

To cite this article: Roel C Kwakernaak *et al* 2026 *Phys. Med. Biol.* **71** 025018

IOP Publishing Phys. Med. Biol. 71 (2026) 025018 https://doi.org/10.1088/1361-6560/ae399e

Physics in Medicine & Biology

IPEM Institute of Physics and Engineering in Medicine

PAPER

Uncertainty analysis in hyperthermia treatment planning for head & neck cancer using polynomial Chaos expansion

Roel C Kwakernaak[1,2,*], **Massimiliano Zanoli**[1], **Zoltan Perkó**[2], **Margarethus M Paulides**[1,3] and **Sergio Curto**[1]

[1] Erasmus MC Cancer Institute, University Medical Center Rotterdam, Department of Radiotherapy, Rotterdam, The Netherlands
[2] Delft University of Technology, Department of Radiation Science and Technology, Delft, The Netherlands
[3] Care+Cure lab of the Electromagnetics group (EM4Care+Cure), Department of Electrical Engineering, Eindhoven University of Technology, Eindhoven, The Netherlands
[*] Author to whom any correspondence should be addressed.

E-mail: r.kwakernaak@erasmusmc.nl

OPEN ACCESS

RECEIVED
16 July 2025

REVISED
28 November 2025

ACCEPTED FOR PUBLICATION
16 January 2026

PUBLISHED
29 January 2026

Keywords: hyperthermia, uncertainty analysis, polynomial Chaos expansion, treatment planning, head and neck cancer, sensitivity analysis

Supplementary material for this article is available online

Abstract

Objective: Hyperthermia, the elevation of tumor temperature to 39 °C–44 °C, is an effective adjuvant treatment for head and neck (H&N) cancer, enhancing the effects of radiotherapy and chemotherapy. This study investigates the robustness of hyperthermia treatment planning (HTP) for H&N cancer using the HyperCollar3D applicator, focusing on uncertainties in patient positioning, tissue properties, and water bolus cooling efficacy. Approach: A retrospective analysis was conducted of 16 patients treated at the Erasmus medical center, utilizing polynomial chaos expansion to model the impact of uncertainties on temperature distributions and treatment quality metrics. Main results: Our findings indicate significant variability in target temperatures due to uncertainties in these tissue properties (2.1 °C T_{90} 95% confidence interval), further exacerbated by patient positioning errors (2.3 °C T_{90} 95% confidence interval for 5 mm positioning errors). Uncertainty in dielectric tissue properties causes the largest chunk of the variance (47%) in T_{90} followed by positioning errors (22%). Significance: This study highlights the critical importance of accurate measurement of tissue properties and precise patient positioning to achieve effective hyperthermia treatment outcomes. Our findings strongly advocate the development of more robust and quantitative treatment planning and delivery approaches, aiming to enhance the precision and clinical efficacy of HTP protocols for H&N cancer treatments.

1. Introduction

Head and neck (H&N) cancer includes a diverse group of cancers that require complex treatment due to the vital functions located in this region. Treatments must balance the achievement of positive oncological outcomes with the management of significant side effects. Standard treatment options include surgery, radiotherapy (RT), and systemic treatments such as chemotherapy (CTx), either alone or in combination de Ridder *et al* (2017). These treatments are often aggressive and cause severe side effects that significantly impact quality of life Hunter *et al* (2020). Despite advances in RT and CTx, mortality for H&N cancer in the Netherlands increased from 867 cases (2012) to 1044 cases (2022), partly due to an aging population Nkr (2023).

Hyperthermia, the elevation of tumor temperature in the range of 39 °C–44 °C, is a potent clinically used adjuvant treatment that enhances the effects of RT and CTx due to several biological effects. The effects of hyperthermia include improved blood perfusion, immune stimulation, reduction of hypoxic areas, and inhibition of DNA repair Evans *et al* (2015), Peeken *et al* (2017), Kok *et al* (2020), which improve tumor damage when combined with RT or CTx. In a study conducted between 2014 and 2018,

22 patients with H&N cancer were treated with hyperthermia plus RT at the Erasmus Medical Center using the HyperCollar3D (HC3D), an in-house developed hyperthermia applicator. The results of this feasibility study were promising Verduijn *et al* (2018), Kroesen *et al* (2021). The HC3D was the first applicator whose design was guided by hyperthermia treatment modeling in the H&N region.

Hyperthermia is generally applied using electromagnetic waves (EM) generated by antennas within the applicator. For phased array applicators, treatments are increasingly being pre-planned using hyperthermia treatment planning (HTP). HTP involves several steps: first, a patient-specific computed tomography (CT) or magnetic resonance imaging (MRI) scan of the treatment area is segmented into separate tissues. Regardless of the origin of the scan, a volumetric (voxel) patient model is created, and the segmented tissues are assigned properties from the literature. The patient model is then virtually placed within the applicator model in the simulation software. Finally, the phases and amplitudes of the antennas in the applicator are determined through power- or temperature-based optimization routines that focus the heating in the target region, for a target-selective temperature elevation Paulides *et al* (2020). Several uncertainties affect the effectiveness of HTP and its translation to the clinical delivery, including variations in patient anatomy, assumptions in heating modeling, and patient positioning. Furthermore, the reported values for the properties of the tissues vary significantly between and within patients Gavazzi *et al* (2020), adding another layer of complexity Paulides *et al* (2021). These uncertainties affect the accuracy of HTP, making it essential to understand their respective impact and manage them for optimal treatment delivery.

Several studies have investigated the impact of these uncertainties on treatment plans. Some have concentrated on uncertainties related to specific tissue properties de Greef *et al* (2010, 2011), Canters *et al* (2013), Groen *et al* (2023), while others have examined the effects of variation in patient position Gellermann *et al* (2007), Canters *et al* (2009), Rijnen *et al* (2015), Aklan *et al* (2017), VilasBoas-Ribeiro *et al* (2022). However, these investigations focused mainly on treatment sites other than the H&N region and considered a limited subset of uncertainties, which may not necessarily be additive. Furthermore, the HC3D stands out as the only clinically used applicator specifically designed for H&N hyperthermia, employing a concentric array of EM sources operating at 434 MHz. Despite these advancements, the literature that addresses the robustness of treatment planning and delivery for the H&N cancers, particularly with microwave-based applicators, remains limited.

In this study, the objective was to assess the robustness of the HTP versus delivery for H&N cancers using the HC3D applicator. Specifically, a retrospective analysis was conducted to evaluate how uncertainties in patient positioning, variations in tissue properties, and the cooling efficacy of the water bolus introduce differences between planned and effectively achieved target temperatures. By examining the influence of these uncertainties on temperature distributions and treatment quality metrics, this study seeks to establish precision requirements for future treatments and provide guidance on acceptable ranges of positioning uncertainties.

2. Materials and methods

2.1. Patient modeling

CT-based models of 16 patients previously treated at Erasmus medical center were included based on data availability from the original cohort of 22. Tumors were located deep (>4 cm depth Kok *et al* (2017), Drizdal *et al* (2023)) in the head (9), deep in the neck (2), superficial on the head (1) and superficial on the neck (4). A uniform 5 mm resolution CT scan was segmented into various tissues by applying the method described in Bellizzi *et al* (2020). Using MATLAB® R2021b (Mathworks) The MathWorks Inc. (2021), a geometry file was generated for each segmented tissue. The tissue geometries that make up the patient model were imported into Sim4Life® (ZMT Zurich MedTech AG) and assigned the properties of the corresponding materials. Temperature and dielectric modeling of the patient was performed according to the ESHO benchmarks proposed by Paulides *et al* (2021). The thermal and dielectric properties of healthy tissue were derived from the IT'IS database Hasgall *et al* (2022). The dielectric properties were extracted at 434 MHz, the operating frequency of the HC3D. Tumor tissue properties were taken based on measurements by Joines *et al* (1994). The nominal values of the tissue properties are listed in table 1. Instead of the perfusion rate, the heat transfer rate is reported, as this is the unit used in Sim4Life®. For both fat and muscle, the heat transfer rate was scaled by a factor of 2.11 and 5.14, respectively, to account for the change in perfusion due to thermal stress Paulides *et al* (2021). To account for cooling caused by breathing, a boundary condition was assigned to the internal air geometries. The air being inhaled was assumed to maintain a constant temperature of 20 °C, and the heat

Table 1. Material properties used in the patient model for a frequency of 434 MHz Joines *et al* (1994), Paulides *et al* (2021), Hasgall *et al* (2022). Values for effective dielectric conductivity (σ), relative dielectric permittivity (ϵ_r), heat-transfer rate (q), and thermal conductivity (k) are given for each of the used tissues in the patient model.

Material	σ (S m^{-1})	ϵ_r (–)	q (W K^{-1} m^{-3})	k (W K^{-1} m^{-1})
Air	0.00	1.00	0.00	0.03
Bone (Cortical)	0.09	13.07	1208	0.32
Brain	1.05	55.11	36 967	0.51
Cartilage	0.60	45.14	2436	0.49
Cerebellum	1.05	55.11	50 932	0.51
Eye (Vitreous humor)	1.53	69.00	0.00	0.59
Fat	0.08	11.59	3979	0.21
Lung	0.38	23.58	9998	0.39
Muscle	0.81	56.87	13 033	0.49
Nerve	0.46	35.04	10 909	0.49
Pons	1.05	55.11	36 967	0.51
Spinal cord	0.46	35.04	10 909	0.51
Thyroid gland	0.89	61.33	373 803	0.52
Tumor	0.88	59.05	6513	0.49

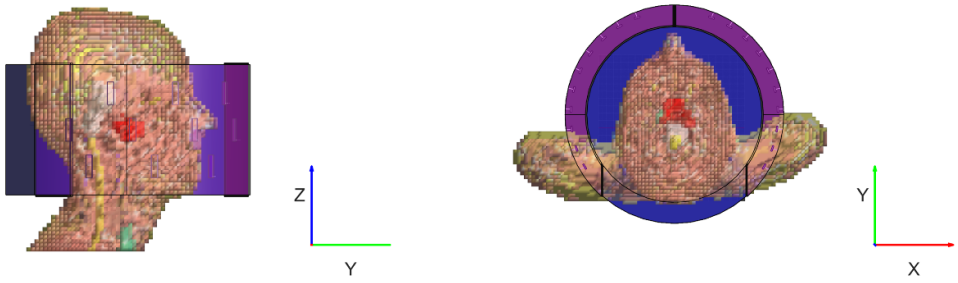

(a) y-z plane (b) x-y plane

Figure 1. Patient and applicator setup in Sim4Life®. The outer bolus is visualized in purple, the inner bolus in blue, and the tumor in red. Axes are included next to each image for clarity.

transfer coefficient at the air-tissue interface was set to 10 W m^{-2} K. The same condition was applied to the external skin/air boundaries between the patient and the background Verhaart *et al* (2015).

2.2. Applicator modeling

The HC3D applicator consists of 20 patch antennas mounted on a cylindrical ground plane and operating at 434 MHz Paulides *et al* (2016). The antennas are immersed in a dedicated outer water bolus enclosed by a thin plastic casing. Between the plastic casing and the patient, an additional inner water bolus, contained in two soft inflatable bags, is inserted for dielectric matching and skin cooling. The applicator model was imported into Sim4Life® and positioned relative to the patient to maximize the margins between the applicator's cylindrical inner surface and the patient's skin in the x-y plane (left-right, back-front), while the position along the z-axis (rostro-caudal) was determined such that the target volume would end up as close as possible to the center of the applicator while preventing the shoulders from intersecting with the solid parts. Figure 1 shows an example of a patient and applicator setup simulated in Sim4Life®. The entire inner cylindrical volume of the applicator was assigned as water, with lower priority than the patient geometries in the voxelization process. This was done to mimic the fact that in clinical practice the inner bolus is inflated as much as possible to prevent air gaps from forming between the patient and the outer bolus. The antennas and ground plate were considered perfect electrical conductors (PEC), and the water boli were assigned pure water dielectric properties ($\epsilon_r = 78.4$, $\sigma = 0.04$ [S m^{-1}]). For the plastic casing, the material properties of Lexan® were used ($\epsilon_r = 3$, $\sigma = 0$ [S m^{-1}]). The inner bolus temperature was set to 30 °C. To account for the cooling of the water bolus, a heat transfer coefficient of 292 W m^{-2} K, derived from Drizdal *et al* (2021), was applied in the simulation. In cases where the tumor was located lower than the mouth, the applicator was tilted 15° around the x-axis, following the clinical protocol Rijnen *et al* (2015).

2.3. Treatment planning

EM simulations were performed using the Sim4Life FDTD solver®. A uniform 1 mm grid was used for the entire region of the applicator model. Outside the applicator model, the grid was graded into a coarse resolution and extended to cover the whole patient model. The grid was further extended with a padding of 50 mm in all directions from the simulated objects. A single layer of Absorbing uniaxial perfectly matched layer boundary conditions was applied at the boundaries of the simulation domain in all directions.

Temperature simulations were performed using the stationary solver of Sim4Life® to obtain the steady-state temperature distribution. A uniform 5 mm grid was used throughout the patient model region, corresponding to the resolution of the patient model. The convergence of temperature metrics with the grid size was added in section A of the supplementary materials (SM), supporting the choice for this grid size. The combined loss distribution from the EM simulation was imported as heat source in the temperature simulation. The stationary solver determines a solution of the Penne's bio-heat equation at steady-state ($\partial T/\partial t = 0$):

$$\nabla\left[k\left(\vec{r}\right)\nabla T\left(\vec{r}\right)\right] + q\left(\vec{r}\right)\left[T_{\mathrm{B}} - T\left(\vec{r}\right)\right] + G\left(\vec{r}\right) + L\left(\vec{r}\right) = 0 \tag{1}$$

where $\vec{r}$ is the domain coordinates, $T(\vec{r})$ is temperature, $k(\vec{r})$ is thermal conductivity, $q(\vec{r})$ is heat-transfer rate, T_{B} is blood temperature (or core body temperature, 37 ,°C), $G(\vec{r})$ ($\mathrm{W\,m^{-3}}$) is heat generated by metabolic activity, and $L(\vec{r})$ ($\mathrm{W\,m^{-3}}$) is externally applied heat, which is equal to the optimized power loss density from the EM simulation. The size of G ($\sim 10^2 - 10^3\,\mathrm{W\,m^{-3}}$) can be considered negligible compared to L ($\sim 10^4 - 10^5\,\mathrm{W\,m^{-3}}$) Gavazzi *et al* (2020), Paulides *et al* (2021), Hasgall *et al* (2022). Furthermore, the mass density $\rho(\vec{r})$ and the specific heat $c(\vec{r})$ do not appear in the steady-state form. Thus, G, ρ, and c were excluded for all tissues from the uncertainty analysis. All tissue properties were modeled as (uncertain) constants, without explicit temperature dependence.

The nominal treatment plan was obtained by importing the individual E-field distributions of the EM simulations into MATLAB®, where a particle swarm algorithm was used to optimize the specific absorption rate (SAR) distribution using the hotspot-target quotient (HTQ) Canters *et al* (2011):

$$\mathrm{SAR} = \frac{L}{\rho} \tag{2}$$

$$\mathrm{HTQ} = \frac{\overline{\mathrm{SAR}}_{R_1}}{\overline{\mathrm{SAR}}_{T}} \tag{3}$$

where $\overline{\mathrm{SAR}}_{R_1}$ is the average SAR in the highest 1-percentile of healthy tissue and $\overline{\mathrm{SAR}}_{T}$ is the average SAR in the target (tumor) tissue. SAR is used for the optimization as a surrogate to temperature Kok *et al* (2018). This provided amplitude and phase settings for each antenna, from which the power loss density distribution L can be determined. This distribution L is used as input for a subsequent temperature simulation, the total power of the heat source was iteratively optimized to achieve a $T_{\max}$ of 44 °C, which is the maximum temperature anywhere in the healthy tissues of the patient, in line with the ESHO benchmarks Paulides *et al* (2021). This provided the nominal scaling factor for the power loss density distribution L. Our approach aligns with the benchmarks and known thermal toxicity thresholds for healthy tissue Yarmolenko *et al* (2011).

2.4. Polynomial Chaos expansion

For the uncertainty analysis, polynomial chaos expansion (PCE) was used, implemented in MATLAB® (version 2021b) Perkó *et al* (2014), The MathWorks Inc. (2021). PCE uses multi-dimensional polynomials (basis vectors $\Psi_n(\vec{\xi})$) in combination with expansion coefficients $r_{i,n}$ to model the response of the temperature distribution ($T_i(\vec{\xi})$ in each voxel i) as a function of the stochastic input variables $\vec{\xi}$, a vector with length equal to the number of considered uncertainty variables N. Each element in the vector $\vec{\xi}$ is a stochastic value retrieved from the joint probability density function of $\vec{\xi}$, and in this study represents a sampled value of the corresponding tissue property, positioning coordinate, or skin/bolus convection coefficient, different from the nominal value. In this study, all elements in $\vec{\xi}$ were considered independent, meaning that the joint probability density function is equal to the product of the individual probability density functions and can be sampled independently. A realization of the stochastic vector $\vec{\xi}$ represents an instance of a possible real treatment and is herein called a scenario. Once the expansion coefficients $r_{i,n}$ are fit on a limited number of known scenarios and corresponding temperature distributions (training set), the PCE model provides a complete description of the stochastic voxel temperature

Table 2. Means and SDs of tissue properties used in the uncertainty analysis using PCE.

	σ (S m^{-1})		ϵ (–)		q (W K^{-1} m^{-3})		k (W K^{-1} m^{-1})	
Tissue	Mean	SD	Mean	SD	Mean	SD	Mean	SD
Bone (Cortical)	0.09	0.02	13.1	2.0	1208	193	0.32	0.03
Brain	1.05	0.26	55.1	8.3	36 967	6551	0.51	0.02
Cartilage	0.60	0.15	45.1	6.8	2436	390	0.49	0.03
Cerebellum	1.05	0.26	55.1	8.3	50 932	8149	0.51	0.03
Eye (Vitreous humor)	1.53	0.38	69.0	10.4	0	0.0	0.59	0.01
Fat	0.08	0.02	11.6	1.7	3980	1563	0.21	0.02
Lung	0.38	0.10	23.6	3.5	9999	8928	0.39	0.09
Muscle	0.81	0.20	56.9	8.5	13 033	4645	0.49	0.04
Nerve	0.46	0.12	35.0	5.3	10 910	2041	0.49	0.03
Pons	1.05	0.26	55.1	8.3	36 967	6552	0.51	0.02
Spinal cord	0.46	0.12	35.0	5.3	10 910	2041	0.51	0.02
Thyroid gland	0.89	0.22	61.3	9.2	373 803	93 247	0.52	0.02
Tumor	0.88	0.22	59.1	8.9	6513	2325	0.49	0.03

response $T(\vec{r}_i, \vec{\xi}) = T_i(\vec{\xi})$ in voxel i as:

$$T_i\left(\vec{\xi}\right) = \sum_{n=0}^{P} r_{i,n} \Psi_n\left(\vec{\xi}\right), \tag{4}$$

where $\Psi_n(\vec{\xi})$ is the nth basis vector and $r_{i,n}$ are the expansion coefficients. The underlying theory supporting PCE is outside the scope of this research but can be reviewed in previous publications Perkó *et al* (2014, 2016).

In this study, all probability density functions were modeled as truncated normal distributions, see section 2.5. Hence, probabilist's Hermite polynomials according to the Wiener–Askey scheme, i.e. orthogonal polynomials, were used as basis vectors for the expansion Xiu and Karniadakis (2002).

2.5. Uncertainty ranges

All uncertainty variables were considered to be normally distributed, with truncations applied to avoid unphysical situations. The means and standard deviation (SD) for tissue properties are given in table 2. The means correspond to the nominal literature values listed in table 1. For σ and ϵ, SD of 25% and 15%, respectively, were chosen, aligned with earlier work Canters *et al* (2013). For both q and k, SDs for each tissue were taken from the IT'IS database Hasgall *et al* (2022). If the SDs was not reported in the database for some tissue, the average ratio of the SDs to the means of the entire database was used to compute a deviation for that tissue. The means and SDs are listed for each tissue in table 2. The distributions were truncated to only positive values for σ. For ϵ, values less than 1 were discarded as this is the value used for ϵ in vacuum. The minimum and maximum values listed in the IT'IS database Hasgall *et al* (2022) were used for both q and k to truncate the normal distributions. The resulting range of the investigated variables is plotted in figure 2.

For positioning uncertainties, a SD of 5 mm was chosen in each 3 directions. Every scenario was checked for realistic positioning, ensuring there was no overlap between the patient and the solid parts of the applicator. Scenarios where overlapping occurred were discarded, resulting in slightly asymmetric actual positioning distributions. Additionally, the impact of increasing positioning uncertainties was also studied, evaluating positioning errors with 95% confidence intervals (CIs) of 0 mm, 3 mm, 5 mm, 10 mm, both on their own (only x, y, z errors) and in combination with all other (tissue property) uncertainties (for more details see section 2.6).

Furthermore, uncertainty in the convection coefficient at the water bolus-skin interface was taken into account, using a mean value of 292 W m^{-2} K and a SD of 80 W m^{-2} K, based on Drizdal *et al* (2021).

2.6. Uncertainty analysis

A polynomial order of 4 was found to be sufficient to accurately describe the response of the temperature to all $N = 56$ uncertainty variables. Using hyperbolic trimming, only the lowest-order cross-terms were preserved in the expansion. These are polynomial terms involving interactions between at most two variables. The other cross-terms were discarded from the expansion to maintain a minimal number of basis vectors as a suitable balance between accuracy and speed, resulting in 1765 basis vector.

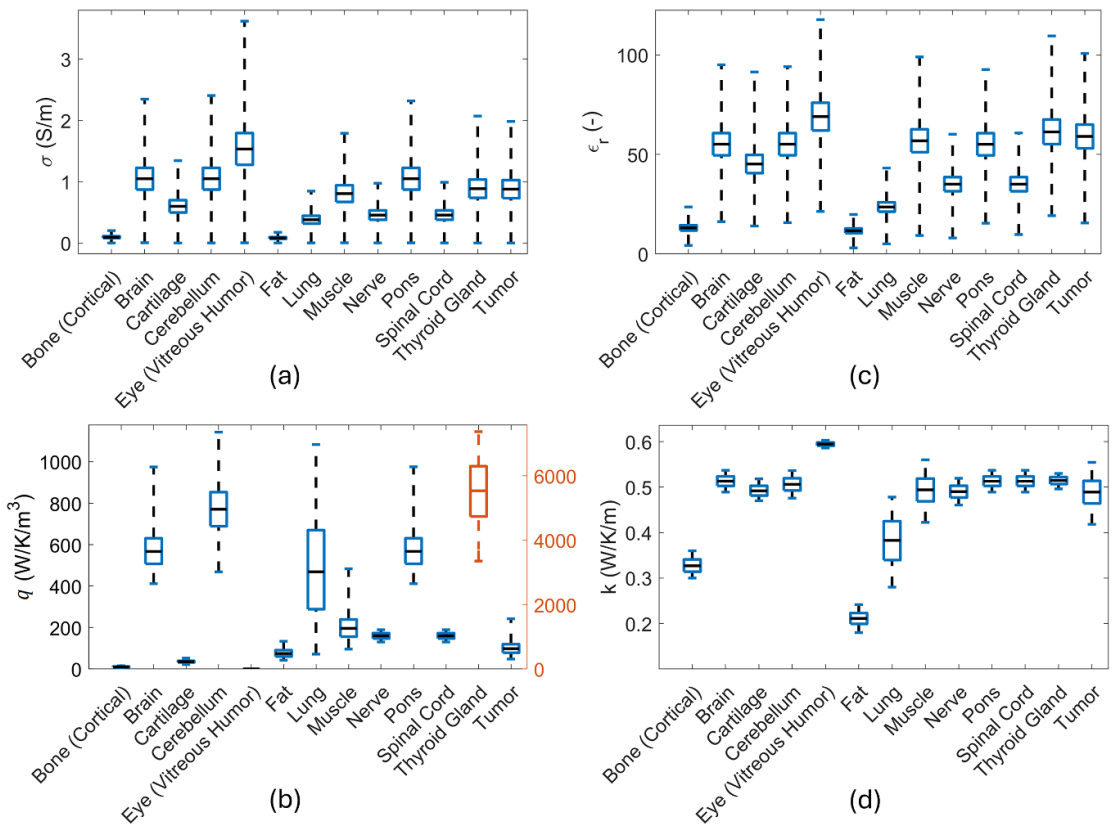

Figure 2. Box-plot showing the median, inter-quartile range and investigated range of (a) dielectric conductivity σ, (b) relative permittivity ϵ_r, (c) heat transfer rate q and (d) thermal conductivity k. Whiskers extend to the minimum and maximum values in the distributions.

To reduce the computational complexity of building the PCE model (i.e. calculating all PCE coefficients), low-impact uncertain variables were excluded from the PCE model based on their individual impact on the temperature distribution. This was done with a preliminary uni-variate analysis, where each uncertainty was simulated with the 2 worst-case values (either ± 3 SD or min and max values as explained in section 2.5). The resulting range on treatment quality metrics ($T_{90}, T_{50}, T_{\max}$) was then calculated using the nominal distribution (distribution obtained with literature values as in planning) and these two extreme scenarios. Uncertainties that had an impact of less than 0.1 °C on all quality metrics were excluded from the analysis. As a result of this approach, the number of remaining basis vectors varied per patient, averaging 272 across the cohort.

For the remaining uncertain variables the PCE model was built using training points generated with random sampling (after discarding points with overlap between patient and solid parts of the applicator), fitting the PCE expansion coefficients with least-squares regression. The number of training points were three times the number of basis vectors in the expansion since no real improvement was found beyond three. This resulted in a total of 815 training points on average for each patient, for which a corresponding number of EM and temperature simulations had to be performed. Further details on the choices regarding the settings of the PCE models, along with data supporting their validity, are provided in section B of the SM.

Clinically, when predicted and actual temperature distributions mismatch due to uncertainties, leading to local hot-spots exceeding the assumed pain or damage threshold of 44 °C, the operator responds by dropping the total power and then gradually increasing it again until either the desired temperature limit is achieved, or the patient experiences discomfort. To mimic this procedure, the total power should be re-optimized for each evaluated scenario such that $T_{\max}$ in healthy tissue becomes 44 °C (similar to what was done in the nominal scenario). However, it was observed that this flattens the temperature response of each voxel and requires a higher polynomial order for accurate PCE modeling. This would increase the computational complexity to the point where the study would no longer be feasible. To circumvent this, a post-processing step was developed and verified to re-scale the temperature distribution after PCE model training. Hence, the PCE models give the voxel-wise dependence of the temperature as a function of the uncertainties assuming that the nominal scenario was scaled to 44 °C maximum

normal tissue temperature, and the post-processing step (described in the next paragraph) models the clinical practice of adjusting power for the given scenario.

After the PCE models were trained for each individual patient in the cohort, 100 000 scenarios were generated by sampling the random distributions of each uncertainty variable in the same way as described in section 2.5. For each scenario $\vec{\xi}$, the corresponding temperature distribution $T(\vec{r},\vec{\xi})$ was quickly determined using the PCE model. Subsequently, the evaluated temperature distribution was re-scaled according to the following linear scheme:

$$\mathrm{T}'\left(\vec{r},\vec{\xi}\right) = \left[T\left(\vec{r},\vec{\xi}\right) - T_0\left(\vec{r}\right)\right]\cdot t + T_0\left(\vec{r}\right) \tag{5}$$

$$t = \frac{44 - T_0\left(\vec{r}_{\mathrm{MAX}}\right)}{T\left(\vec{r}_{\mathrm{MAX}}\right) - T_0\left(\vec{r}_{\mathrm{MAX}}\right)} \tag{6}$$

$$\vec{r}_{\mathrm{MAX}} = \arg\max_{\vec{r}\in H}\left[T\left(\vec{r}\right)\right], \tag{7}$$

where $T'\left(\vec{r},\vec{\xi}\right)$ is the re-scaled temperature distribution, $T_0(\vec{r})$ is the baseline temperature distribution (temperature simulation with zero EM power and nominal values for all uncertain variables), and H is the set of voxels belonging to healthy tissue. In this way, the temperature distributions for 100 000 randomly sampled error scenarios per patient were corrected to achieve 44 °C as a maximum temperature anywhere in the healthy tissue, reflecting the clinical procedure. We validated this method of scaling the temperature distribution in section C of the SM.

To assess the impact of increasing positioning errors, multiple 95% CIs were analyzed for patient positioning. Specifically, CIs of 0 mm, 3 mm, 5 mm, and 10 mm were evaluated. The SD for positioning in the x, y, and z directions were derived by dividing the specified CI by $\sqrt{\chi^2_{3,0.95}}$, where $\chi^2_{3,0.95}$ is the critical value of the chi-squared distribution with three degrees of freedom at the 95% confidence level. Note that this resulted in having to sample in a smaller domain than the scenarios used for training the PCE models with $SD = 5$ mm in each 3 directions.

Statistics to compare distributions were calculated using a T-student test.

2.7. Sensitivity analysis

Finally, a variance-based global sensitivity analysis (Sobol analysis Sobol (2001)) was conducted to assess the relative influence of each uncertainty variable on the 90th percentile target volume temperature T_{90} (i.e. the maximum temperature that at least 90% of the target volume has). A separate set of PCE-generated scenarios was used to compute first-order Sobol indices for each variable $n \in N$ for each patient. In addition to the individual parameter Sobol indices, an analysis was performed where the variables were grouped into four categories (positioning, dielectric tissue properties, thermal tissue properties and water bolus convection coefficient) to determine first order group Sobol sensitivity indices for each 4 groups of parameters Jacques *et al* (2006), Prieur and Tarantola (2017). First order group Sobol indices allow us to evaluate the combined effect of a subset of variables on T_{90}, taking into account the interaction and potential correlations between all variables within the group.

To estimate all first order Sobol indices, the classical Monte Carlo estimator was employed, sometimes also called pick-freeze method Gamboa *et al* (2013), which defines a structured sampling scheme to evaluate the effect of each input variable (or variable group). Using this method, 100 sets of 1000 scenarios were sampled for each variable. For the group indices 1000 sets of 1000 scenarios were sampled for each group. The corresponding T_{90} values were computed using the PCE model (and post-processing re-scaling), exploiting its speed to make the computations feasible. The resulting T_{90} distributions were used to estimate the first-order Sobol indices via the conditional expected value operator E and variance operator V, according to:

$$S_n = \frac{V_{\vec{\xi}_n}\left\{E_{\vec{\xi}_{\sim n}}\left[T_{90}\left(\vec{\xi}_{\sim n}\right)|\vec{\xi}_n\right]\right\}}{V\left\{T_{90}\left(\vec{\xi}\right)\right\}}, \tag{8}$$

for each variable (group) n.

3. Results

Figure 3 illustrates the impact of uncertainty on the temperature distribution at the target plane. The nominal temperature distribution (figure 3(a)) obtained during planning closely resembles the mean distribution (figure 3(b)) observed in the evaluation of 100 000 error scenarios. Figure 3(c) shows that the

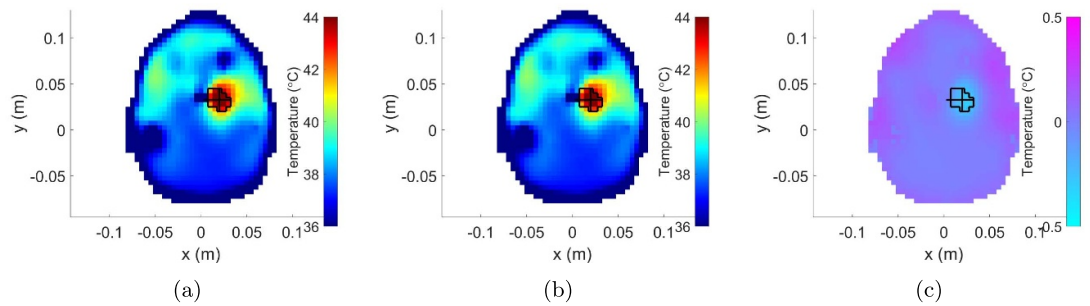

Figure 3. x-y section through the center of the target for (a) nominal (b) mean and (c) mean deviation of temperature distribution from the nominal distribution in deep head patient 1 (nominal is subtracted from mean distribution). The target is delineated in a dashed black contour.

largest temperature variations occur inside the target and at the hot-spots in healthy tissue. In particular, the impact of the uncertainties is, on average, a general reduction of the target temperatures, while hot-spot temperatures tend to become higher.

Figure 4 illustrates how varying levels of positional uncertainty, combined with differences in tissue properties, influence the 95% CI of the temperature volume histogram (TVH). In particular, a significant spread in the delivered target temperature is observed even in the absence of positional uncertainty, highlighting the inherent target temperature variance introduced by tissue properties. The inclusion of positional uncertainty further widens the CI, with larger positioning errors increasing this effect. Individual differences in sensitivity to positioning errors are observed as the magnitude of this impact varies across patients.

Table 3 shows that the range in quality metrics T_{90} and T_{50} increases with worsening CI in patient positioning in combination with uncertainty in tissue properties and water bolus cooling efficacy. Compared with perfect positioning (0 mm), a 5 mm/95% induces an additional 0.4 °C and 0.3 °C in the 95% CI of T_{90} and T_{50}, respectively. These values increase to 1.0 °C when the positioning is within 10 mm/95%.

Table 3 also shows that when considering uncertainties in positioning only (i.e. assuming that all tissue properties and bolus cooling coefficient are known exactly), CI increases with 0.7 °C and 0.8 °C for the T_{90} and T_{50}, respectively, for positioning within 3 mm/95% (compared to perfect positioning). This CI increases to 2.2 °C and 2.1 °C, respectively, when positioning is only within 10 mm/95%. For further details about the probability density functions of the T_{90} and T_{50} with and without positioning errors (for an example patient) see section D of the SM.

The nominal, median and 95% CI for the T_{90} and T_{50} are visualized in figure 5 for the entire patient cohort. The median and mean T_{90} and T_{50} from the PCE evaluation closely matched the nominal planning values. A statistical comparison of the distributions across the population showed no significant difference ($p > 0.05$), indicating that the expected values of the quality metrics were roughly equal to the nominal values observed in the planning.

Figure 6 shows how different variables contribute to the variance of T_{90} assuming a positioning error of 5 mm / 95% CI. Among the positioning variables the largest individual impact is often due to a translation along x, which is expected since the antennas of the HC3D are arranged at the left (negative x) and right (positive x) sides, while leaving openings in the back (negative y) and front (positive y) of the patient. Among all tissue properties, the dielectric properties (ϵ, σ) of muscle and tumor consistently appear among the 10 variables having the highest impact on T_{90}. The bolus convection coefficient h becomes relevant only for some of the superficial targets.

Figure 7 shows how groups of variables collectively contribute to the variance of T_{90}, again assuming a positioning error of 5 mm / 95%. On average, across the entire patient cohort, the overall positioning error Δr together with tissue dielectric properties together contribute to 69% of the total variance of T_{90}. The bolus convection coefficient h becomes relevant only for the sub-group of patients having a superficial target. Results for the other positioning evaluations (3 mm / 95% and 10 mm / 95%) for both the first order as well as the group Sobol indices can be found in section D of the SM.

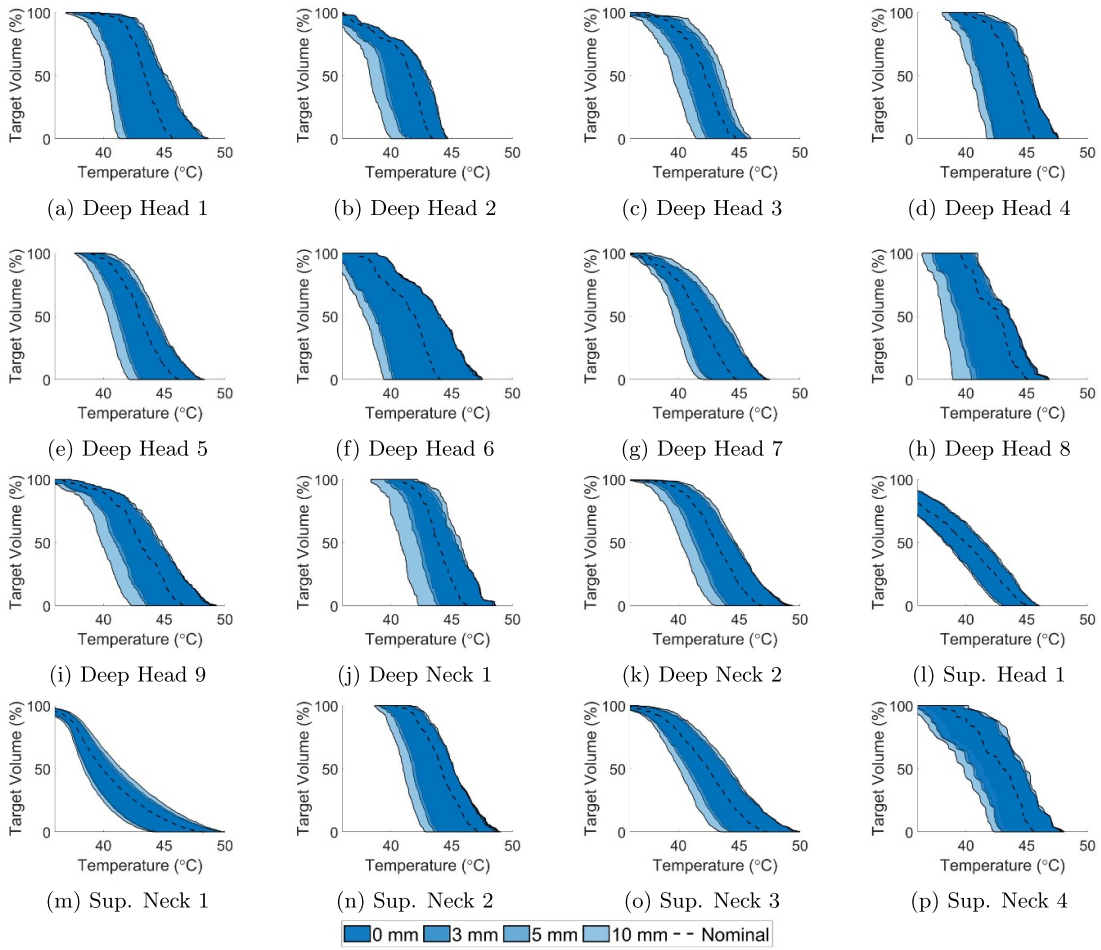

Figure 4. TVH with 95-CI bands for a 100 000 scenario evaluations using different CI for positioning in x, y, z of 0 mm, 3 mm/95%, 5 mm/95% and 10 mm/95% for each patient.

Table 3. Comparison of the average range of the 95% CI for T_{50} and T_{90} in the patient population using different 95% CI for patient positioning when combined with all other uncertainties. The impact of patient positioning alone is also reported when all other uncertainties are assumed to be zero.

Metric	0 mm	3 mm / 95%	5 mm / 95%	10 mm / 95%
T_{90}	2.1	2.2	2.4	3.1
T_{50}	2.7	2.8	3.0	3.6
T_{90} (only x, y, z)	0.0	0.7	1.2	2.2
T_{50} (only x, y, z)	0.0	0.8	1.2	2.1

4. Discussion

The primary objective of this study was to evaluate the relative impact of delivery uncertainties in hyperthermia treatments for the H&N region with the HC3D applicator. The inclusion of a large number of uncertainty variables was enabled by a tailored approach based on PCE. A large target temperature variance was observed due to uncertainty in tissue properties alone. This variance increases when errors in patient positioning were also accounted for.

Performing a proper selection of input variables and their probabilistic modeling is crucial in any uncertainty analysis. In this study, the input uncertainties for the tissue properties are based on measurements reported in the IT'IS Hasgall *et al* (2022) database, which rely primarily on *ex-vivo* data. Tissue properties from this database may not fully capture the unique perfusion and thermal conductivity dynamics of the H&N region, as suggested by Verhaart *et al* (2015). Despite these limitations, the values provided in this study provide a starting point to model an anatomical region for which otherwise there is little or no literature, and assess the relative impact of the different uncertainties.

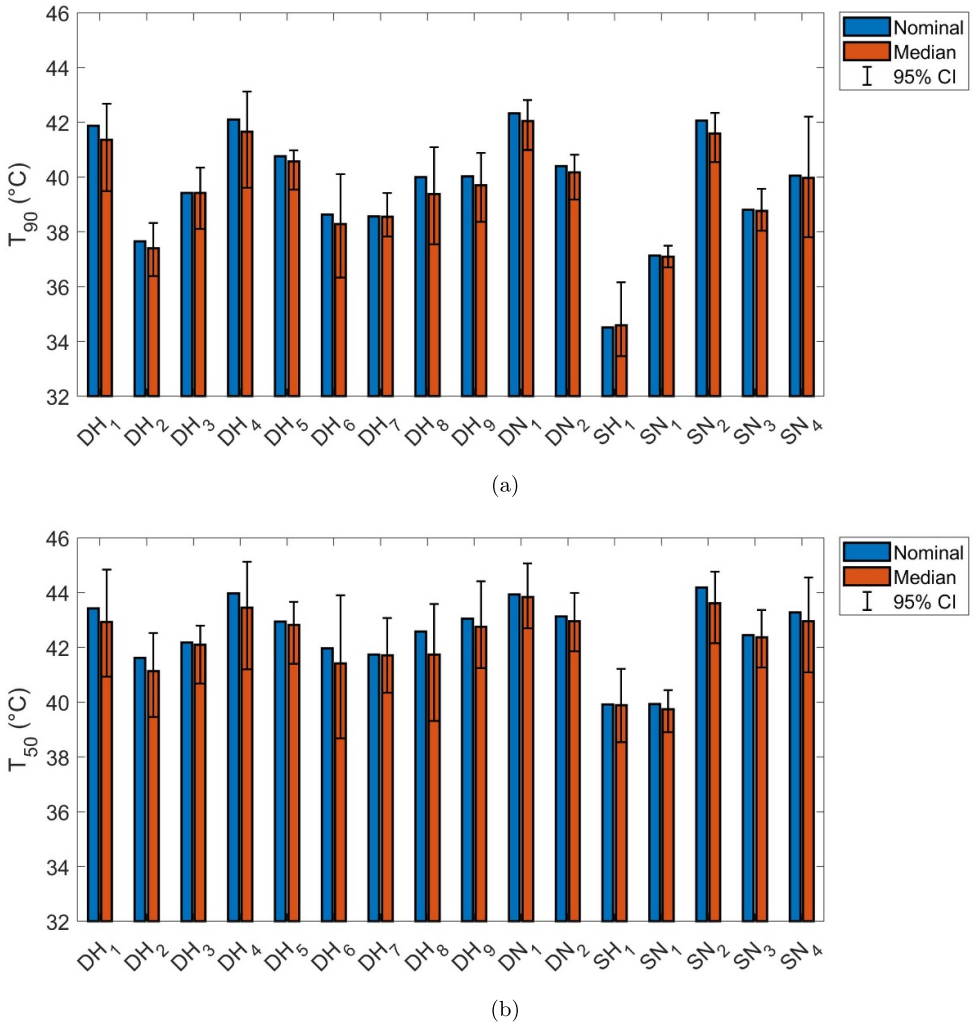

Figure 5. Bar chart illustrating (a) T_{90} and (b) T_{50} for patients categorized as deep head (DH), deep neck (DN), superficial head (SH), and superficial neck (SN). The chart presents nominal and median values derived from the 100 000-scenario PCE evaluation assuming a positioning error of 5 mm / 95%, with error bars indicating the 95% CI.

In addition, perfusion was modeled using static thermal stress factors as recommended by the ESHO benchmarks Paulides *et al* (2021), which do not provide an explicit reference temperature but fall within the physiologically observed hyperthermic range. While perfusion is inherently temperature-dependent Song (1984), Drizdal *et al* (2018), steady-state formulations can be interpreted as using an equivalent static perfusion value that yields the same thermal dose as a fully transient model, given that hyperthermia dose is defined as an integral of temperature over time. By sampling perfusion values across the expected physiological range, a substantial part of the possible temporal behavior might implicitly be represented. Spatially non-linear perfusion responses may still influence mid-range temperatures (particularly those relevant for T_{50} and T_{90}) but this is expected to be a second-order effect. Moreover, conducting fully transient simulations for the complete training set is currently computationally infeasible. As such, steady-state simulations with static perfusion scaling remain consistent with accepted practice in uncertainty quantification for hyperthermia Groen *et al* (2023).

In light of this, it is important to note that the absolute values reported in the quality metrics (e.g. table 3) cannot be interpreted as definitive predictions. However, the relative uncertainties derived from the analysis are based on simulated instances reflecting expected deviations and, as such, provide meaningful insights. This approach is supported by findings such as those of Kok *et al* (2018) who demonstrated that predicted relative temperature changes align well with the measured thermal response of patients during hyperthermia treatments. Consequently, while absolute values are limited by inherent property mismatches between literature data and reality, relative differences provide more reliable indications on where the research efforts should focus on to improve treatment quality.

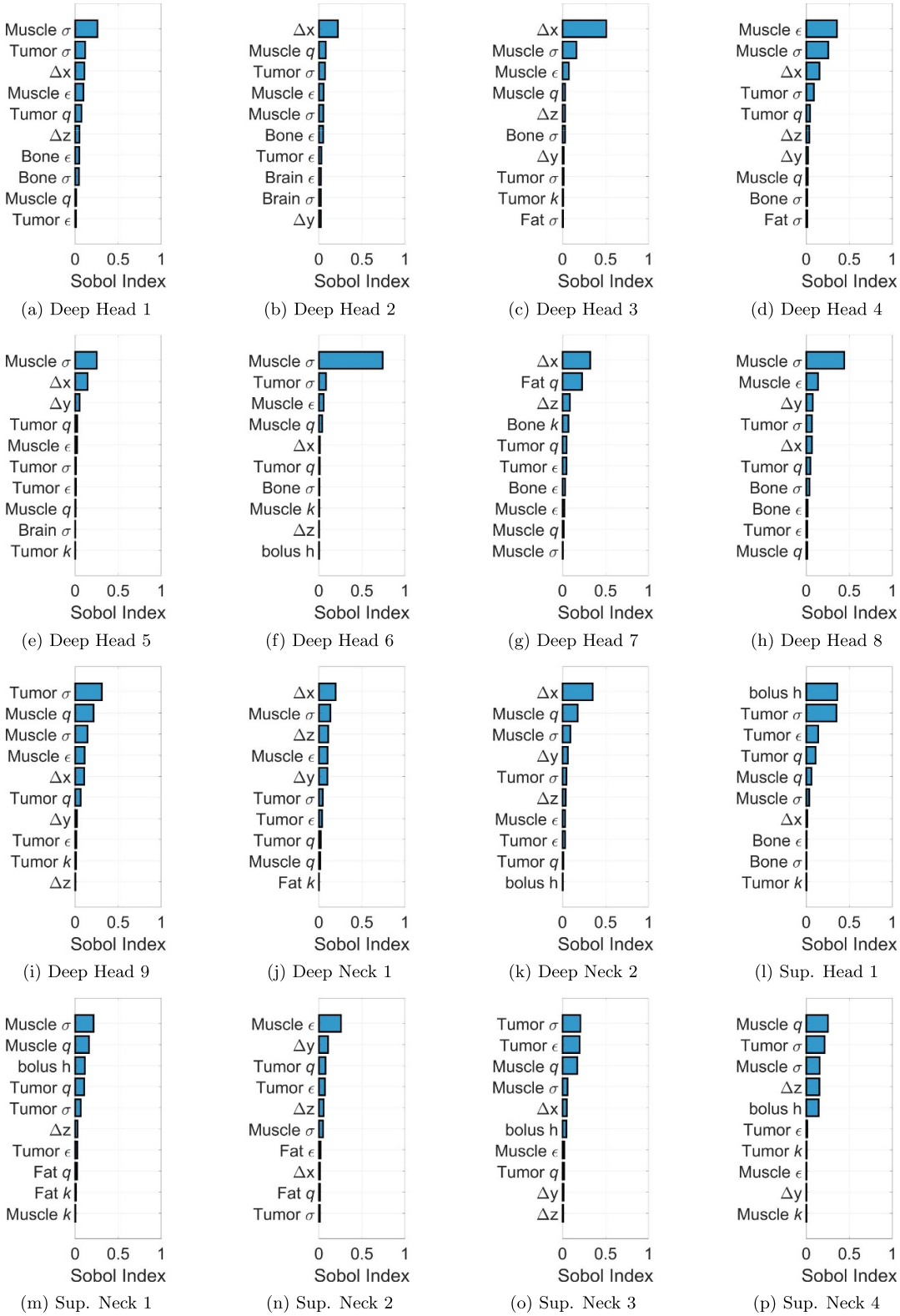

Figure 6. The 10 highest first-order Sobol indices for each patient, calculated for T_{90} with a 5 mm / 95% positioning uncertainty.

Our method adjusts the temperature distribution to ensure a maximum of 44 °C in healthy tissue across all error scenarios. This adjustment prevents unrealistic outcomes by addressing two key issues: (1) excessively high hot-spots, which are mitigated by reducing power in response to pain complaints, and (2) suboptimal temperatures below 44 °C, corrected by increasing power to maintain treatment efficacy. Since both approaches are commonly used in clinical practice, the proposed method is considered to closely mirror real-world treatment conditions.

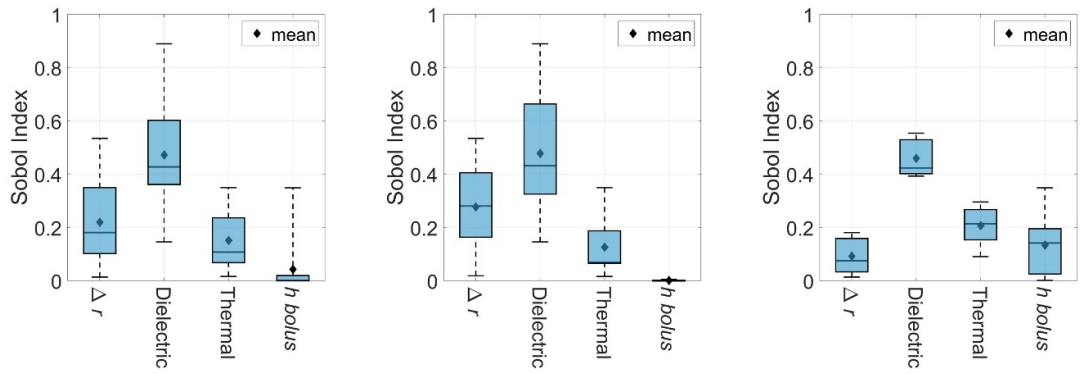

(a) All Patients (16) (b) Deep (11) (c) Superficial (5)

Figure 7. Boxplots of first-order group Sobol indices for the following categories: positioning (Δr), dielectric tissue properties, thermal tissue properties, and water bolus convection coefficient (h). Sobol indices are calculated for T_{90} under a 5 mm / 95% positioning uncertainty. Patients are further sub-grouped according to target location. Whiskers extend to the minimum and maximum values, the box spans the interquartile range, the median is shown inside the box, and the mean is indicated by a diamond marker.

In this study, the water bolus was modeled as a uniform cylinder of water. However, in practice, deviations in the water bolus shape and air bubbles may occur that can alter the heating pattern. Rijnen *et al* estimated that differences in the shape of the water bolus could cause up to 20% variation in the HTQ (2015). Although this uncertainty was not explicitly addressed here,the heat transfer coefficient h at the interface between skin and water was included in th analysis, since its value is also not entirely known for temperature simulations Van Der Gaag *et al* (2006). Variations in h were determined to have a relevant impact only for patients with a superficial tumor, while its effect on deep seated targets is negligible. Overall, the water bolus remains a complex component difficult to model in treatment planning and statistical assessment, and improved design solutions are still sought after. Other sources of uncertainty not addressed in the current study include the number of segmented tissues and segmentation errors.

From the uncertainty analysis, it was observed that quality metrics have large CIs, even when the patient is perfectly positioned. For example, the combined impact of all considered uncertainty variables on T_{90} is a 95% CI of 2.4 °C under 5 mm / 95% positioning, and this CI reduces by 0.3 °C to 2.1 °C when no positioning error is present. Conversely, introducing tissue property uncertainty to a case with only positioning error increases the CI by 1.3 °C. As shown in table 3, the ranges in T_{50} are consistently about 0.6 °C larger than those for T_{90} across all positioning levels, when all uncertainties are included. This indicates that T_{50} is more sensitive to uncertainty, while T_{90} is relatively more stable. This is an encouraging result since T_{90} has been most consistently linked to clinical outcome Ademaj *et al* (2022).

From the sensitivity analysis, it was found that positioning errors (5 mm / 95%), on average, account for about 22% of the total variance in T_{90}. The bulk of the variations are uncertainties in tissue properties (62%), with dielectric properties representing the largest chunk (47%). Higher order interactions between the groups represent a smaller ($\approx 10\%$) part of the variance. With less accurate positioning (10 mm / 95%) it naturally becomes a bigger source of uncertainty, accounting for 45% of the total variance (see section D of the SM). Moreover, this variance is not uniform across all patients, as large variations in individual cases are observed. For some patients, positioning errors alone can contribute up to 53% of the total variance in T_{90}, highlighting the need for patient-specific considerations in treatment planning. Based on this study, the hyperthermia target volume in the TANCA-I trial (ClinicalTrials.gov ID: NCT06761937) was defined as the gross target volume with an added 5 mm margin. These findings motivate the development of improved methods for patient registration and *in-vivo* tissue property characterization at treatment time. Quantitative microwave imaging is a good candidate to address both issues Rubæk *et al* (2007), Semenov (2009), as it provides online maps of tissue permittivity and conductivity in a non-invasive manner. Other indirect approaches such as model fitting from invasive/intraluminal thermometric probes or MRI-based measurements could also improve accuracy Cheng and Plewes (2002), Verhaart *et al* (2015).

The Sobol analysis provides valuable information on the uncertainties that most significantly contribute to the variance in treatment quality metrics. As seen in figure 6, for some patients, the variance is primarily influenced by a subset of variables. This information could prove useful when optimizing

treatment plans for robustness, as it suggests that accounting for only a limited number of variables may suffice, rather than considering all potential factors. In particular, for deep-seated tumors, the number of key influencing variables appears smaller than superficial tumors. This difference may be attributed to the more intricate cooling processes involved in superficial treatments.

5. Conclusion

This work demonstrates the impact of uncertainties between HTP and delivery for the H&N region. Most of the variance in target temperatures is caused by uncertainties in tissue properties, but this variance increases when uncertainties in positioning are also considered. The study consolidates the need for more accuracy in hyperthermia treatments and motivates further research on how to improve patient positioning and develop *in-vivo* tissue property measurement methods. Last, the results also indicate that robust treatment planning approaches—similar to charged particle RT planning—might benefit hyperthermia treatments too.

PCE can be a powerful framework to investigate the impact of different input of uncertainties. Future work might involve the use of PCE to compare different optimization methods for treatment planning, defining the accuracy required for techniques such as non-invasive image guidance, and aiding in the development of probability-based methods for treatment planning.

Data availability statement

The data cannot be made publicly available upon publication because they are not available in a format that is sufficiently accessible or reusable by other researchers. The data that support the findings of this study are available upon reasonable request from the authors.

Supplementary Materials available at https://doi.org/10.1088/1361-6560/ae399e/data1.

Acknowledgments

This research was supported by KWF Kankerbestrijding (Dutch Cancer Society) under project number 15018 (RADIATHE) and Eurostars project 3868 (SENS-THERM). The authors would like to thank Michiel Kroesen for reviewing this manuscript from a clinical perspective.

Credit authorship contribution statement

Roel C. Kwakernaak: Methodology, Software, Validation, Formal Analysis, Investigation, Data Curation, Writing—Original Draft, Visualization.

Massimiliano Zanoli: Conceptualization, Methodology, Software, Formal Analysis, Investigation, Data Curation, Writing—Review and Editing, Supervision.

Zoltán Perkó: Methodology, Software, Formal Analysis, Writing—Review and Editing, Supervision.

Margarethus M. Paulides: Conceptualization, Writing—Review and Editing.

Segio Curto: Supervision, Project Administration, Funding Acquisition, Resources, Writing—Review and Editing.

ORCID iDs

Roel C Kwakernaak 0009-0008-7509-1847
Massimiliano Zanoli 0000-0002-3149-6905
Zoltan Perkó 0000-0002-0975-4226
Margarethus M Paulides 0000-0002-5891-2139
Sergio Curto 0000-0002-3073-1117

References

Ademaj A *et al* 2022 Clinical evidence for thermometric parameters to guide hyperthermia treatment

Aklan B, Gierse P, Hartmann J, Ott O J, Fietkau R and Bert C 2017 Influence of patient mispositioning on sar distribution and simulated temperature in regional deep hyperthermia *Phys. Med. Biol.* **62** 4929

Bellizzi G G, Sumser K, VilasBoas-Ribeiro I, Curto S, Drizdal T, van Rhoon G C, Franckena M and Paulides M M 2020 Standardization of patient modeling in hyperthermia simulation studies: introducing the erasmus virtual patient repository *Int. J. Hyperth.* **37** 608–16

Canters R A M, Franckena M, Paulides M M and Van Rhoon G C 2009 Patient positioning in deep hyperthermia: influences of inaccuracies, signal correction possibilities and optimization potential *Phys. Med. Biol.* **54** 3923

Canters R A, Paulides M M, Franckena M, Mens J W and van Rhoon G C 2013 Benefit of replacing the sigma-60 by the sigma-eye applicator. a monte carlo-based uncertainty analysis *Strahlenther. Onkol.* **189** 74–80
Canters R, Franckena M, van der Zee J and Rhoon G 2011 Optimizing deep hyperthermia treatments: are locations of patient pain complaints correlated with modelled sar peak locations? *Phys. Med. Biol.* **56** 439–51
Cheng H-L M and Plewes D B 2002 Tissue thermal conductivity by magnetic resonance thermometry and focused ultrasound heating *J. Magn. Reson. Imaging* **16** 598–609
de Greef M, Kok H P, Correia D, Bel A and Crezee J 2010 Optimization in hyperthermia treatment planning: the impact of tissue perfusion uncertainty *Med. Phys.* **37** 4540–50
de Greef M, Kok H P, Correia D, Borsboom P P, Bel A and Crezee J 2011 Uncertainty in hyperthermia treatment planning: the need for robust system design *Phys. Med. Biol.* **56** 3233–50
de Ridder M *et al* 2017 Variation in head and neck cancer care in the netherlands: a retrospective cohort evaluation of incidence, treatment and outcome *Eur. J. Surg. Oncol. (EJSO)* **43** 1494–502
Drizdal T, Paulides M M, van Holthe N and van Rhoon G C 2018 Hyperthermia treatment planning guided applicator selection for sub-superficial head and neck tumors heating *Int. J. Hyperth.* **34** 704–13
Drizdal T, van Rhoon G C, Fiser O, Vrba D, van Holthe N, Vrba J and Paulides M M 2023 Assessment of the thermal tissue models for the head and neck hyperthermia treatment planning *J. Therm. Biol.* **115** 103625
Drizdal T, van Rhoon G C, Verhaart R F, Fiser O and Paulides M M 2021 A guide for water bolus temperature selection for semi-deep head and neck hyperthermia treatments using the hypercollar3d applicator *Cancers* **13** 6126
Evans S S, Repasky E A and Fisher D T 2015 Fever and the thermal regulation of immunity: the immune system feels the heat *Nat. Rev. Immunol.* **15** 335–49
Gamboa F, Janon A, Klein T, Lagnoux-Renaudie A, Prieur C, and Prieur C, 2013 Statistical inference for sobol pick freeze monte carlo method (arXiv:1303.6447)
Gavazzi S, van Lier A L H M W, Zachiu C, Jansen E, Lagendijk J J W, Stalpers L J A, Crezee H and Kok H P 2020 Advanced patient-specific hyperthermia treatment planning *Int. J. Hyperth.* **37** 992–1007
Gellermann J, Göke J, Figiel R, Weihrauch M, Cho C H, Budach V, Felix R and Wust P 2007 Simulation of different applicator positions for treatment of a presacral tumour *Int. J. Hyperth.* **23** 37–47
Groen J A, Crezee J, van Laarhoven H W M, Bijlsma M F and Kok H P 2023 Quantification of tissue property and perfusion uncertainties in hyperthermia treatment planning: multianalysis using polynomial chaos expansion *Comput. Methods Programs Biomed.* **240** 107675
Hasgall P A, Di Gennaro F, Baumgartner C, Neufeld E, Lloyd B, Gosselin M C, Payne D, Klingenböck A, and Kuster N 2022 IT'IS database for thermal and electromagnetic parameters of biological tissues (available at: https://itis.swiss/database)
Hunter M, Kellett J, Toohey K, D'Cunha N M, Isbel S and Naumovski N 2020 Toxicities caused by head and neck cancer treatments and their influence on the development of malnutrition: review of the literature *Eur. J. Investig. Health Psychol. Educ.* **10** 935–49
Jacques J, Lavergne C and Devictor N 2006 Sensitivity analysis in presence of model uncertainty and correlated inputs *Reliab. Eng. Syst. Saf.* **91** 1126–34
Joines W T, Zhang Y, Li C and Jirtle R L 1994 The measured electrical properties of normal and malignant human tissues from 50 to 900 mhz *Med. Phys.* **21** 547–50
Kok H P, Cressman E N K, Ceelen W, Brace C L, Ivkov R, Grüll H, ter Haar G, Wust P and Crezee J 2020 Heating technology for malignant tumors: a review *Int. J. Hyperth.* **37** 711–41
Kok H P, Korshuize-van Straten L, Bakker A, de Kroon-Oldenhof R, Geijsen E D, Stalpers L J A and Crezee J 2017 Online adaptive hyperthermia treatment planning during locoregional heating to suppress treatment-limiting hot spots *Int. J. Radiat. Oncol. Biol. Phys.* **99** 1039–47
Kok H P, Schooneveldt G, Bakker A, de Kroon-Oldenhof R, Korshuize-van Straten L, de Jong C E, Steggerda-Carvalho E, Geijsen E D, Stalpers L J A and Crezee J 2018 Predictive value of simulated sar and temperature for changes in measured temperature after phase-amplitude steering during locoregional hyperthermia treatments *Int. J. Hyperth.* **35** 330–9
Kroesen M, van Holthe N, Sumser K, Chitu D, Vernhout R, Verduijn G, Franckena M, Hardillo J, van Rhoon G and Paulides M 2021 Feasibility, sar distribution and clinical outcome upon reirradiation and deep hyperthermia using the hypercollar3d in head and neck cancer patients *Cancers* **13** 6149
Nkr T 2023 Mortality by year data retrieved from NKR (available at: https://nkr-cijfers.iknl.nl/)
Paulides M M, Rodrigues D B, Bellizzi G G, Sumser K, Curto S, Neufeld E, Montanaro H, Kok H P and Trefna H D 2021 ESHO benchmarks for computational modeling and optimization in hyperthermia therapy *Int. J. Hyperth.* **38** 1425–42
Paulides M M, Trefna H D, Curto S and Rodrigues D B 2020 Recent technological advancements in radiofrequency-andmicrowave-mediated hyperthermia for enhancing drug delivery *Adv. Drug. Deliv. Rev.* **163-164** 3–18
Paulides M M, Verduijn G M and Van Holthe N 2016 Status quo and directions in deep head and neck hyperthermia *Radiat. Oncol.* **11** 21
Peeken J C, Vaupel P and Combs S E 2017 Integrating hyperthermia into modern radiation oncology: what evidence is necessary? *Front. Oncol.* **7** 132
Perkó Z, Gilli L, Lathouwers D and Kloosterman J L 2014 Grid and basis adaptive polynomial chaos techniques for sensitivity and uncertainty analysis *J. Comput. Phys.* **260** 54–84
Perkó Z, van der Voort S R, van de Water S, Hartman C M H, Hoogeman M and Lathouwers D 2016 Fast and accurate sensitivity analysis of impt treatment plans using polynomial chaos expansion *Phys. Med. Biol.* **61** 4646
Prieur C and Tarantola S 2017 *Variance-Based Sensitivity Analysis: Theory and Estimation Algorithms* (Springer) pp 1217–39
Rijnen Z, Togni P, Roskam R, van de Geer S G, Goossens R H M and Paulides M M 2015 Quality and comfort in head and neck hyperthermia: a redesign according to clinical experience and simulation studies *Int. J. Hyperth.* **31** 823–30
Rubæk T, Meaney P M, Meincke P and Paulsen K D 2007 Nonlinear microwave imaging for breast-cancer screening using gauss–newton's method and the cgls inversion algorithm *IEEE Trans. Antennas Propag.* **55** 2320–31
Semenov S 2009 Microwave tomography: review of the progress towards clinical applications *Phil. Trans. R. Soc. A* **367** 3021–42
Sobol I 2001 Global sensitivity indices for nonlinear mathematical models and their monte carlo estimates *Math. Comput. Simul.* **55** 271–80
Song C W 1984 Effect of local hyperthermia on blood flow and microenvironment: a review *Cancer Res.* **44** 4721s–30s
The MathWorks Inc. 2021 Matlab version: 9.11.0.1769968 (r2021b) Natick, Massachusetts, United States (available at: www.mathworks.com)

Van Der Gaag M L, De Bruijne M, Samaras T, Van Der Zee J and Van Rhoon G C 2006 Development of a guideline for the water bolus temperature in superficial hyperthermia *Int. J. Hyperth.* **22** 637–56

Verduijn G M, de Wee E M, Rijnen Z, Togni P, Hardillo J A U, ten Hove I, Franckena M, van Rhoon G C and Paulides M M 2018 Deep hyperthermia with the hypercollar system combined with irradiation for advanced head and neck carcinoma—a feasibility study *Int. J. Hyperth.* **34** 994–1001

Verhaart R F, Verduijn G M, Fortunati V, Rijnen Z, van Walsum T, Veenland J F and Paulides M M 2015 Accurate 3d temperature dosimetry during hyperthermia therapy by combining invasive measurements and patient-specific simulations *Int. J. Hyperth.* **31** 686–92

VilasBoas-Ribeiro I, Franckena M, van Rhoon G C, Hernández-Tamames J A and Paulides M M 2022 Using mri to measure position and anatomy changes and assess their impact on the accuracy of hyperthermia treatment planning for cervical cancer *Int. J. Hyperth.* **40** 2151648

Xiu D and Karniadakis G E 2002 The wiener–askey polynomial chaos for stochastic differential equations *SIAM J. Sci. Comput.* **24** 619–44

Yarmolenko P S, Moon E J, Landon C, Manzoor A, Hochman D W, Viglianti B L and Dewhirst M W 2011 Thresholds for thermal damage to normal tissues: an update *Int. J. Hyperth.* **27** 320–43